PYROCLASTICS NORTHEAST OF GASSENDI CRATER: DISCOVERY/CHARACTERISTICS/ IMPLICATIONS. T.A. Giguere[1], B.R. Hawke[1], D. Trang[1], L.R. Gaddis[2], S.J. Lawrence[3], J.D. Stopar[4], J.O. Gustafson[5], J.M. Boyce[1], J.J. Gillis-Davis[1], and the LROC Science Team[6]. [1]Hawaii Institute of Geophysics and Planetology, Univ. of Hawaii, Honolulu, HI 96822, [2]U.S. Geological Survey, Astrogeology Science Center, Flagstaff, AZ 86001, [3]Johnson Space Center, Houston, TX, [4]Lunar and Planetary Institute, Houston, TX, [5]Cornell Univ., Ithaca, NY 14850, [6]School of Earth and Space Exploration, Arizona State Univ., Tempe, AZ 85281 (giguere@hawaii.edu).

Introduction: In our ongoing effort to better understand lunar volcanism on the Moon, we are investigating pyroclastic deposits in the Gassendi region. Interest in pyroclastics has remained high due to the availablility of high-resolution data (LRO, Kaguya), which is used to build on previous remote sensing studies [e.g., 1, 2, 3] and also extensive studies of lunar pyroclastic glasses [4, 5]. Analyses conducted in the laboratory of pyroclastic spheres from several deposits show that this volcanic material had a greater depth of origin and lesser fractional crystallization than mare basalts [e.g., 4, 6]. Data indicates that pyroclastic glasses are the best examples of primitive materials on the Moon, and they are important for both characterizing the lunar interior and as a starting place for understanding the origin and evolution of lunar basaltic magmatism [2].

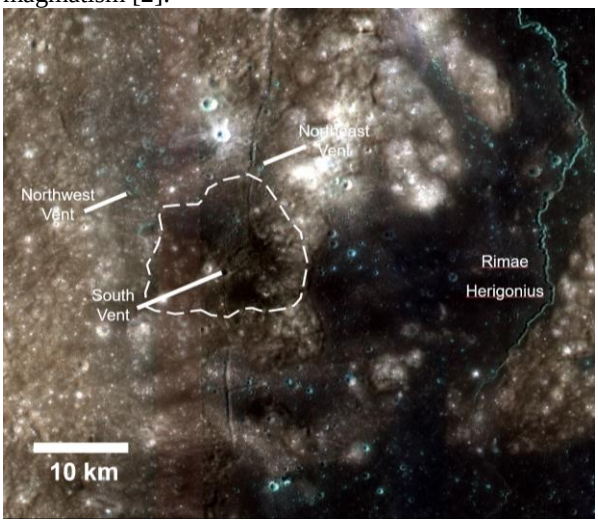

***Figure 1**. Northeast pyroclastics and three vents (arrowed). The white-dashed outlines the primary deposit. Data from the Kaguya Multiband Imager, with a spatial resolution of ~20 m/pixel [18]; false-color view (red=band 3, 900 nm; green=band 2, 700 nm; blue=band 1, 415 nm). North is up.*

We analyzed Lunar Reconnaissance Orbiter Camera (LROC) Wide Angle Camera (WAC) and Narrow Angle Camera (NAC) images, Kaguya imagery, as well as other spacecraft data, to conduct a survey of the Gassendi region to search for previously unidentified pyroclastic deposits [e.g., 3]. Multiple pyroclastic deposits and associated vents were identified to the northeast of Gassendi crater. These deposits are examined with the methodologies established by recent workers based on the latest spacecraft data [3, 7, 8]. The purposes of this study are as follows: (1) To identify and characterize previously unknown localized pyroclastic deposits, (2) To determine the composition of the pyroclastic units, (3) To measure deposit block populations, thicknesses and in turn the volume, (4) To investigate the eruption mechanisms responsible for the emplacement of these dark mantle deposits.

Data and Methods: Both LROC WAC (high and low incidence) and NAC images were used in this investigation [9, 10]. Topographic data were provided by the LROC GLD100 [11] digital topographic model (DTM). The LRO Diviner Lunar Radiometer Experiment seven band (~8-300 μm) rock abundance map data at 128 m/pixel [12, 13], which reveals blocks on the surface >1 m, was obtained for this study.

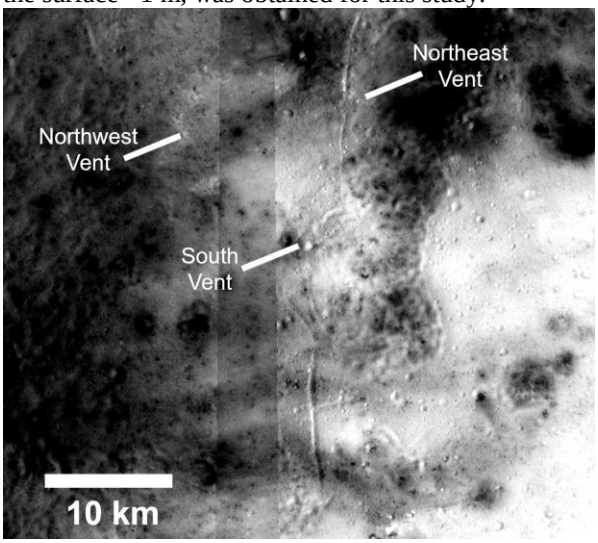

***Figure 2.** Northeast pyroclastics and three vents (arrowed). Kaguya MI FeO image. North is up.*

The Clementine 5-color UV-VIS digital image model (DIM; [14]) were used to produce OMAT, FeO and TiO_2 maps [15, 16] and for 5-point spectra.

Image data from the (JAXA) SELENE "Kaguya" monochromatic Terrain Camera [17] and the Multiband Imager [18] visible and N multispectral camera were used for detailed surface and geochecmical analysis. The thickness and volume of the localized pyroclastic deposit was calculated from the Wide Angle Camera (WAC) and Kaguya digital terrain models (DTM) using methods similar to [19]. The deposit thickness was determined by modeling the pre-erupted

surface, then subtracting each pixels from the DTM of the pyroclastic deposit. The maximum deposit thickness was determined from the largest pixel difference.

Results and Discussion:

The pyroclastic deposit shown in Figure 1, is located ~45 km to the northeast of the NW Gassendi crater rim at 15.0°S 37.7°W with the dark mantling deposit subtending an area of ~20x20 km. Marshall [20] produced the USGS I-385 map, which shows the terrain is largely Imbrium-aged Regional material (Ir) with possible "Procellarian"-aged (now Upper Imbrian) mare at the south end of the pyroclastic. We know that Marshall had some doubts about mapping this area as mare since there is a "?" shown after the label. A lineament is mapped through the deposit, which is interpreted as a fault or fracture. Our results find that the previously mapped mare material, while dark in albedo, is a dark mantling deposit which blankets hills and depressions in the area. Pyroclastic material is observed on the hills east of the main deposit, which is 1000 meters higher in elevation. Currently available high-resolution NAC data provides a detailed view of the lineament which is roughly parallel to Rima Herigonius to the east; the lineament is less sinuous than the Herigonius rille thus is more likely to be a structural feature.

Three vents have been located, two are north of the main deposit (Northwest vent, Northeast vent), while the South vent is in the mapped pyroclastic deposit, Figure 1. The Northwest vent (14.8°S, 38.1°W) is 800 x 500 m and is line with a northwest-southeast trending rille. The Northeast vent (14.7°S, 37.7°W) is in line with the north-south rille, is roughly circular (1.4 x 1.4 km) and has an adjoining linear vent section to the north. The South vent is the largest of the three, roughly rectangular in shape, and is 3 x 2 km in size. At 120 m the South vent is the deepest of the three vents.

The Kaguya [18] and Clementine [15, 16] geochemical datasets were examined to understand the composition of the pyroclastics deposits. The entire area shows elevated FeO value (i.e. >12 wt%) and the defined pyroclastic region (white dashed area in Figure 1) exhibits FeO values averaging 14-16, with the highest values approaching 17 wt% (Figure 2). This area of elevated values continues to the north of the other two vents, however, is interrupted by a secondary crater chain which disrupts the regolith and lowers the Fe values. The distribution of TiO_2 matches the distribution of the Fe-rich material. The highest TiO_2 values range between 3 and 4 wt%.

A sample area to the northwest of the South vent was selected to determine the rock abundance in the pyroclastic deposit. This area was largely free of fresh craters, which tend to excavate and distribute blocky material. The mean surface rock abundance for this deposit is 0.30% with a standard deviation of 0.10%. This surface rock abundance value is within the range determined for 34 pyroclastic deposits of 0.24–0.54% with a mean of 0.38% and a standard deviation of 0.09% by Trang et al. [8]. These values may be compared to the modal rock abundances for regional pyroclastic deposits, highlands, and maria are 0.3, 0.4, and 0.5%, respectively [13].

Color ratio images (Figure 3) cancel out the dominant brightness variations in multispectral scenes caused by albedo variations and topographic shading and serve to isolate the color variations related to minerology or maturity (e.g. 21, 22). Immature highlands presents as aqua, iron-rich volcanic materials are yellowish, and both impact melts [22] and glassy Fe^{2+}-rich pyroclastics [21] appears as deep red in a color ratio image. The South vent area has no large, fresh impacts nearby, thus impact melt is not present; glass rich pyroclastics blanket and surround the South vent. Additional confirmation is planned using Kaguya mineral mapping techniques [23].

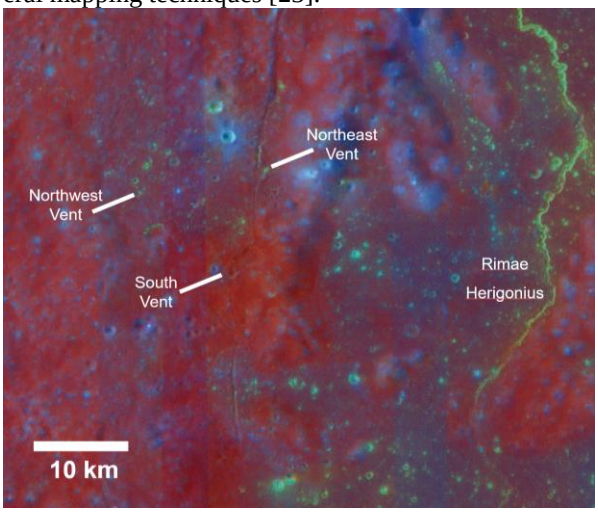

Figure 3. *Northeast pyroclastics and three vents (arrowed). Kaguya MI color-ratio (red=750/415, green=750/950, blue=415/750 nm). North is up.*

References: [1] Gaddis L. et al. (1985) Icarus, 61, 461. [2] Gaddis, L. et al. (2003) Icarus, 161, 262-280. [3] Gustafson, O. et al. (2012) JGR, 117, E00H25. [4] Shearer C. and Papike J. (1993) GCA, 57, 4785. [5] Hagerty J. et al. (2006) GCA, 70, 3457. [6] Papike J. et al. (1998) Revi. Miner., 36, 5.1. [7] Gaddis, L. et al. (2016) LPSC XLVII, #2065. [8] Trang, D et al. (2017) Icarus, 283, 232-253. [9] Robinson, M. et al., (2010) Spac Sci. Rvw 150, 81. [10] Speyerer, E. et al., (2011) LPSC XLII, #2387. [11] Scholten F. et al. (2012) JGR, 117, 12 pp. [12] Paige et al. (2010), Space Sci. Rev., 150, 125-160. [13] Bandfield et al. (2011), JGR, 116, E00H02. [14] Eliason E. et al. (1999) LPS XXX, #1933. [15] Lucey P. et al. (2000) JGR, 105 (E8), 20,297. [16] Lucey P. et al. (2000) JGR, 105 (E8), 20,377. [17] Haruyama et al. (2008) Earth Plan. Space, 60, 243– 256. [18] Ohtake, M. et al. (2008) Earth Plan. Space, 60, 257-264. [19] Head J. W. and Wilson L. (1979), Proc. Lunar Sci. Conf. 10th, 10, 2861–2897. [20] Marshall C. (1963) U.S.G.S. Map I-385. [21] Pieters, C.M. et al. (1994) Science, 266, 1844. [22] McEwen, A.S. et al. (1994) Science, 266, 1858. [23] Lemelin, M. et al. (2015) JGR, 120, 869-887.